

Effect of adhesive interaction on strain stiffening and dissipation in granular gels undergoing yielding

Sebanti Chattopadhyay¹, Sharadhi Nagaraja^{1,2} & Sayantan Majumdar ¹✉

Shear induced yielding in disordered solids, characterized by irreversibility and enhanced dissipation, is important for a wide range of industrial and geological processes. Although such phenomena in thermal systems have been extensively studied, they remain poorly understood for granular solids. Here, using oscillatory shear rheology we study energy dissipation in a disordered solid formed by dense granular suspensions of adhesive frictional particles. We find non-linear flow regimes showing intra-cycle strain stiffening and plasticity that strongly depend on both the applied strain amplitude and particle volume fraction, which can be captured by the normalized energy dissipation. Furthermore, in-situ optical imaging reveals irreversible particle rearrangements correlating with the spatio-temporal fluctuations in local velocity across the yielding transition. By directly measuring the critical jamming packing fraction using particle settling experiments, we propose a phase diagram that unravels the effect of inter-particle interactions on flow properties of the system for a large parameter space.

¹Soft Condensed Matter Group, Raman Research Institute, Bengaluru 560080, India. ²Department of Physics and Materials Science, Université du Luxembourg, L-1511 Luxembourg, Luxembourg. ✉email: smajumdar@rri.res.in

Diverse disordered materials close to jamming show a finite elasticity under small perturbations. When the applied perturbations become large enough, plasticity and irreversible deformations take place as the material yields^{1–4}. Yielding in amorphous solids plays an important role in material processing industries as well as catastrophic natural phenomena like landslides and earthquakes^{5,6}. Yielding also implies an enhanced energy dissipation^{3,7} that eventually leads to fluidization/fracture of the material. As opposed to crystalline systems, due to lack of translational symmetry there is no obvious structural precursor (similar to crystalline defects) of yielding for disordered materials^{8,9}. This makes the understanding of yielding phenomena in amorphous solids particularly challenging.

In recent years there have been extensive studies, both experimental and theoretical, to understand failures in amorphous materials^{3,10–30}. Many of these studies are motivated by the generalized jamming phase diagram describing yielding in a variety of disordered materials based on only a few control parameters³¹. Dense particulate suspensions have been widely used as model systems for studying the yielding behavior in such systems. Depending on the inter-particle interactions, these systems show striking non-linear flow properties like, yielding, shear-thinning, shear-thickening, and shear-induced jamming^{32–37}.

Although, yielding and failure in glassy and gel-like materials formed by Brownian particles have been widely studied, experiments probing the same in non-Brownian granular suspensions of rigid particles are very few^{38–40}. Besides being inherently out of equilibrium, the main complexity arises from the fact that due to the large size of the constituent particles, flow of granular materials are dominated by contact interactions, since the stress scale for contact formation (critical onset stress) between two repulsive particles, $\sigma^* \propto 1/d^2$ (d : particle diameter)⁴¹. Moreover, close to jamming, the average surface to surface separation between two particles becomes negligible compared to the particle size. As a result, van der Waals and other short-ranged attractive/adhesive interactions become very important for granular systems⁴². All these contributions make the flow behavior of these systems extremely complicated.

To cut through the complexity arising due to the frictional and adhesive/attractive interactions between non-Brownian particles, recently proposed constraint rheology models have been quite successful^{43–46}. In these models, all the interactions are encoded in the jamming packing fraction for the system, which gradually decreases from the value obtained in the limit of hard-core steric repulsion as the sliding and rolling degrees of freedom for the particles become more and more constrained due to enhanced inter-particle interactions. Measuring the jamming packing fractions from numerical simulations and using a generalized version of Wyart–Cates model⁴⁷, the framework of constraint rheology successfully captures many experimental aspects of yielding in granular systems. The complex interplay between inter-particle adhesion and friction demonstrated in recent experimental studies^{44,45} emphasizes the difference in yielding mechanism in adhesive granular and Brownian systems, despite some superficial similarities in rheological response. Such difference mainly originates from the inter-particle friction that plays a far more important role in case of granular systems as compared to their Brownian counterparts. It is also evident from these studies that the existing framework of Brownian systems is not sufficient to describe yielding in adhesive non-Brownian systems and a fresh perspective is required.

In adhesive systems, stress-induced viscoelastic deformation of fractal clusters can also play a key role in determining the mechanical properties. Such deformations can reflect as quasi-reversible strain stiffening response in bulk rheological measurements as has also been observed in colloidal gels^{48–50}.

Importantly, in granular systems, deformations of fractal particle clusters involve both adhesive and frictional contacts between the particles. Since the number of these contacts depends on both applied perturbation and particle volume fraction, the strain stiffening response should also depend on these parameters. However, a detailed study of strain stiffening and its correlation with inter-particle interactions in the context of yielding in adhesive granular systems is currently lacking. The origin of such non-linearities also remains beyond the existing theoretical models for these systems. Such understanding is particularly crucial in the light of the difference in microscopic mechanism of yielding in colloidal and granular systems as mentioned above. All these points further signify that the nature of strain stiffening in granular systems can be quite distinct and the existing studies on colloidal systems are not sufficient to capture the detailed strain-stiffening phenomena in adhesive granular systems. Furthermore, both thermal and athermal systems of attractive/adhesive particles show significant strain-localization which gets enhanced with increasing strength of interaction, as shown by recent experimental and simulation studies^{51–58}. However, any possible connection between strain-stiffening and spatio-temporal variation of velocity gradients in the system has not been highlighted in these studies. Thus, a complete picture of the yielding behavior requires the bulk non-linearity and energy dissipation to be connected to the local strain distribution, particle-scale interactions and irreversibility in these systems.

Here, we study non-linear mechanics, energy dissipation, and plasticity in soft solids formed by dense granular suspensions of cornstarch particles in paraffin oil over a wide range of particle volume fractions and applied strain amplitudes. We find that the normalized energy dissipation and intra-cycle strain stiffening show a non-monotonic variation that depends on both strain amplitude, as well as, particle volume fractions. To our knowledge, such complex behavior has never been reported in the context of yielding in granular or colloidal gels. To gain a microscopic insight we experimentally determine critical jamming packing fractions for the adhesive granular system. These critical parameters encode complex, many-body interparticle interactions in the system and also automatically take into account the amorphous shape of the particles. We further show that these critical parameters can explain the complete flow behavior of the system, as described in the detailed phase diagram.

Results and discussion

Dense suspensions are prepared by dispersing cornstarch (CS) particles in paraffin oil for different volume fractions ϕ (see the section “Materials and methods”). CS particles are amorphous having mean-diameter $\approx 15 \mu\text{m}$ with a polydispersity of 30% (Fig. S1). The particles have an average Young’s modulus $\approx 5 \text{ GPa}$ (see ref. ⁵⁹ and references therein) and can be considered to be rigid (see the section “Materials and methods”). For rheological measurements, we perform oscillatory amplitude sweep at a constant frequency (see the section “Materials and methods”). We show the variation of Elastic (G') and Viscous (G'') moduli as a function of strain amplitude (γ_0) for $\phi = 0.4$ in Fig. 1a. The system remains predominantly elastic ($G' > G''$) till intermediate γ_0 . For larger strain amplitudes, a crossover to fluidization is observed with $G'' > G'$. However, we do not find any linear visco-elastic region (where G' and G'' become independent of γ_0) even for γ_0 values as low as 0.0001 (see Fig. S2a). This implies that some rearrangements are always present in the system. In fact, we also find an absence of linear response regime for suspensions of CS particles dispersed in a density matched hydrophobic organic liquid (see the section “Materials and methods” and Fig. S2b) as well. This indicates that such behavior is not caused by density

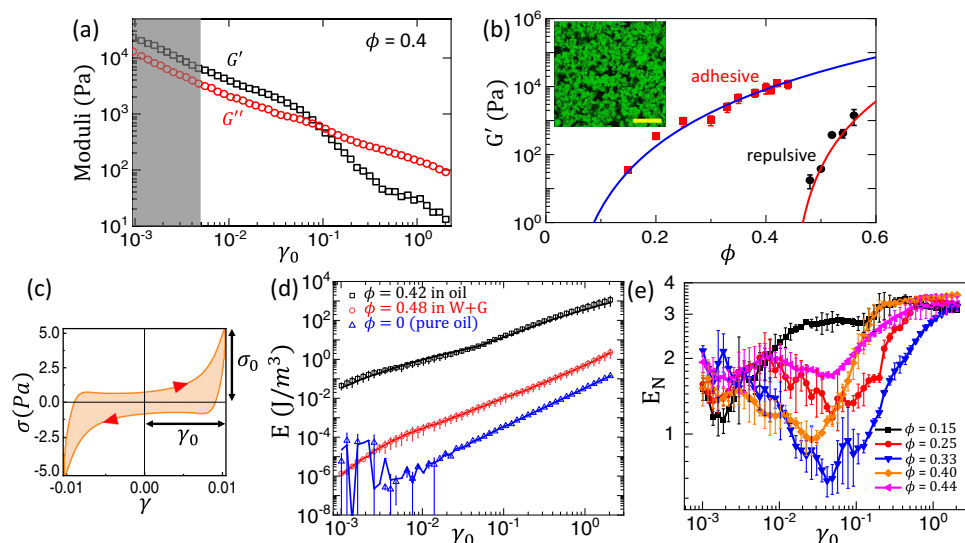


Fig. 1 Variation of energy dissipation of the system across yielding transition. **a** Typical variation of elastic (G') and viscous (G'') moduli as a function of applied strain amplitude (γ_0) for cornstarch (CS) particles dispersed in Paraffin oil for a volume fraction (ϕ) = 0.4. The data shown correspond to a single measurement. **b** G' vs. ϕ for CS in water (black circles) and CS in Paraffin oil (red squares). The error bars represent the standard deviation of G' values over the range of γ_0 indicated by the shaded region in panel **(a)**. The solid lines are fits to the empirical relation $G' = G_\phi(\phi - \phi_j)^\alpha$ (ϕ_j is the jamming volume fraction of the system) with $\alpha = 5.1$, $\phi_j = 0.02$ for CS in oil and $\alpha = 4.6$, $\phi_j = 0.44$ for CS in water. Inset shows maximum intensity projection of typical confocal z-stack images for CS in oil system inside a gravitationally settled bed. Scale bar: 150 μm . **c** A typical elastic Lissajous plot (orange curve) showing intra-cycle strain stiffening. The peak stress σ_0 and strain amplitude γ_0 for the Lissajous plot are also indicated. The bounding box denotes the Lissajous plot for an ideal plastic material for the same σ_0 and γ_0 . **d** Variation of dissipated energy density (E) as a function of γ_0 for CS in oil ($\phi = 0.42$), CS in water-glycerol mixture ($\phi = 0.48$) and pure solvent (oil) as indicated by different symbols. The solid lines indicate $E = \pi \gamma_0^2 G''$ and the error bars are the standard deviation from two independent measurements. **e** Normalized energy dissipation (E_N) as a function of γ_0 for different ϕ values indicated in the figure. Data points represent the mean values and error bars represent the standard deviations of at least three independent experimental runs (except for $\phi = 0.15$, where only two runs are considered).

mismatch. This non-linear response is further confirmed by significant contribution of the higher harmonics of G' (Fig. S3). In some cases we observe noticeable even harmonic values, as also reported for highly non-linear polymeric systems⁶⁰. However, we find that for repeated experimental runs, the average even harmonic contributions remain negligible compared to the odd harmonics (Fig. S3).

To study the effect of inter-particle interactions in controlling the mechanical properties of the system under small perturbations, we plot G' values averaged over strain amplitude range $0.001 < \gamma_0 < 0.005$ (shaded region in Fig. 1a) for different ϕ values in case of both adhesive (CS in oil) and repulsive (CS in water) suspensions in Fig. 1b. We find that the adhesive interactions give rise to significant elasticity at ϕ values much lower compared to that required for the repulsive suspension to have a similar elasticity, as has been observed in numerical simulations⁵⁴ and other experimental studies⁶¹ as well. For adhesive inter-particle interactions, contact networks comprising of fractal aggregates (Fig. S4 and Supplementary note 1) impart stability to the system for average coordination numbers well below the Maxwell isotacticity criterion⁶². Using confocal imaging (see the section “Materials and methods”) we indeed observe such a system spanning porous structure inside a stable bed settled under gravity (inset, Fig. 1b and also Supplementary Movies 1 and 2). These porous structures are stabilized by the adhesive interactions to support their own weight which also explains the origin of bulk elasticity in the system for volume fractions far below the random close packing limit (≈ 0.56) obtained in the presence of steric repulsion alone⁶³. As expected, we see that such porous structures are not stable under gravity in presence of steric-repulsive inter-particle interactions alone (Supplementary Movies 1 and 2). We observe that the variation of G' as a function of ϕ is compatible with a proposed empirical law⁶¹: $G' = G_\phi(\phi - \phi_j)^\alpha$ for both

adhesive and repulsive suspensions (Fig. 1b). However, we find that the exponent α and the parameter ϕ_j are different for these two suspensions. This is not surprising, since, these parameters depend on detailed inter-particle interactions, as also observed earlier⁶¹.

For different ϕ values, we also record intra-cycle stress (σ) vs. strain (γ) for each data point of G' , G'' vs. γ_0 to obtain Lissajous plots. One such plot is depicted in Fig. 1c showing a clear signature of non-linear strain stiffening when the differential shear modulus $K = \frac{d\sigma}{d\gamma}$ increases with increasing strain. The area enclosed by the Lissajous plot gives the intra-cycle energy dissipation per unit volume (dissipated energy density): $E = \oint \sigma(\gamma) d\gamma$. We compare the variation of E as a function of γ_0 for both adhesive (CS in oil) and repulsive suspensions (CS in water-glycerol mixture) in Fig. 1d. We observe that E increases monotonically with increasing γ_0 as well as ϕ values (see Fig. S5). Importantly, we see that the dissipated energy for the adhesive system remains several orders of magnitude higher than that for the repulsive system over the entire strain range. CS particles are hydrophilic, so when dispersed in paraffin oil, they form an adhesive suspension (see the section “Materials and methods”). We should note that in both repulsive (CS in water, see the section “Materials and methods”) and attractive/adhesive (CS in paraffin oil) suspensions, steric repulsion is present but additionally in case of attractive/adhesive suspensions, the particles stick together on contact and there is an energy cost to break such contacts. This explains the hugely enhanced dissipation in the attractive/adhesive system compared to the repulsive one. In all cases, we find that the analytical expression $E = \pi G'' \gamma_0^2$ captures the variation of the dissipated energy accurately (Fig. 1d). However, in our case G'' is not a constant but decreases with γ_0 roughly as a power law over the entire range of strain amplitudes

(Fig. 1a). This implies $E \sim \gamma_0^\alpha$ with the exponent $\alpha < 2$, unlike the case of pure viscous or linear visco-elastic materials⁷ ($\alpha = 2$).

We find that dissipated energy E , which has a monotonic dependence on both γ_0 and ϕ , does not provide much information about the non-linearity in the system, as indicated by the self-similar nature of the curves in Fig. S5. Thus, to capture the non-linearity and dissipation in the system over a wide range of parameters, we define normalized energy dissipation (see ref. 64 and references therein), $E_N = \frac{E}{\sigma_0 \gamma_0}$, where σ_0 is the peak stress corresponding to an applied strain amplitude γ_0 . Physically, the quantity $4\sigma_0 \gamma_0$ denotes the dissipation for an ideal plastic material as indicated by the bounding box in Fig. 1c. We plot the variation of E_N as a function of γ_0 over a range of ϕ values (Fig. 1e). We find that E_N shows a non-monotonic variation as a function of both γ_0 as well as ϕ . The decrease in E_N with increasing γ_0 arises due to the strain stiffening behavior shown by the system (Fig. 1c). Similar strain stiffening and plasticity is also observed for the density matched system (Fig. S2b) mentioned earlier. These observations demonstrate that our experimental results for adhesive granular suspensions are independent of gravity induced effects.

We now take a closer look at the non-monotonicity of E_N to understand the yielding behavior of the system. Figure 2a shows the typical variation of E_N as a function of γ_0 for CS in oil system ($\phi = 0.4$). For small γ_0 , the average value E_N is denoted by E_N^0 . With increasing γ_0 , the value of E_N first decreases from E_N^0 and reaches a minimum. At intermediate values of γ_0 , E_N increases and becomes larger than E_N^0 , finally saturating beyond $\gamma_0 \geq 0.2$ for the higher γ_0 values (Fig. 2a). In the region where $E_N \leq E_N^0$, the system displays strain stiffening response which disappears in the region with $E_N > E_N^0$, where the mechanical response shows strain-weakening/plasticity as indicated by the Lissajous plots in Fig. 2d–g. For soft viscoelastic solids under an oscillatory shear,

the yield strain is defined by the critical strain amplitude beyond which the elastic modulus G' starts to drop from its constant (linear response) value⁶⁵. This yield point is usually close to the crossover point of G' and G'' (flow point). Since in our system we do not find a linear response regime even for strain values far below the flow point as seen in Fig. 1a (also, Fig. S2a), the yield strain in our case cannot be defined by the conventional manner. Also, as our system is highly non-linear, the fundamental harmonics (G' and G'') alone are not sufficient to capture the flow behavior accurately. Hence, we define the yield strain as the strain amplitude (γ_y) beyond which the normalized dissipation E_N exceeds E_N^0 as indicated in Fig. 2a. We find that γ_y comes fairly close to the flow point (Fig. S6). Beyond γ_y (indicated in Fig. 2a), the dissipation in the system shows a significant increase as shown by the Lissajous plots in Fig. 2d–g. Similar enhancement of dissipation beyond the yielding transition has also been observed earlier¹⁵.

Next, we look at the flow behavior of the system by mapping out the velocity profiles across the shear gap using boundary imaging during the applied oscillatory deformations. The schematic of rheology and in-situ optical imaging set-up of the sample boundary is shown in Fig. S7. Due to the opaque nature of particles, we can image only a thin layer of sample near the suspension–air interface. Since we apply an oscillatory strain, instantaneous velocity of the moving bottom plate v_0 continuously increases from 0 to v_{\max} over one quarter of a sinusoidal cycle of strain deformation (measured from a turning point). Here, v_{\max} is the maximum plate velocity for a given strain amplitude γ_0 : $v_{\max} = \omega \gamma_0 d$ (d : shear gap, ω : angular frequency). We show the velocity profiles across the shear gap obtained from a single measurement for few discrete values of v_0 varying between 0 to v_{\max} for two different γ_0 values in Fig. 2b ($\gamma_0 = 0.04$) and 2c ($\gamma_0 = 0.5$), corresponding to the two regions identified in

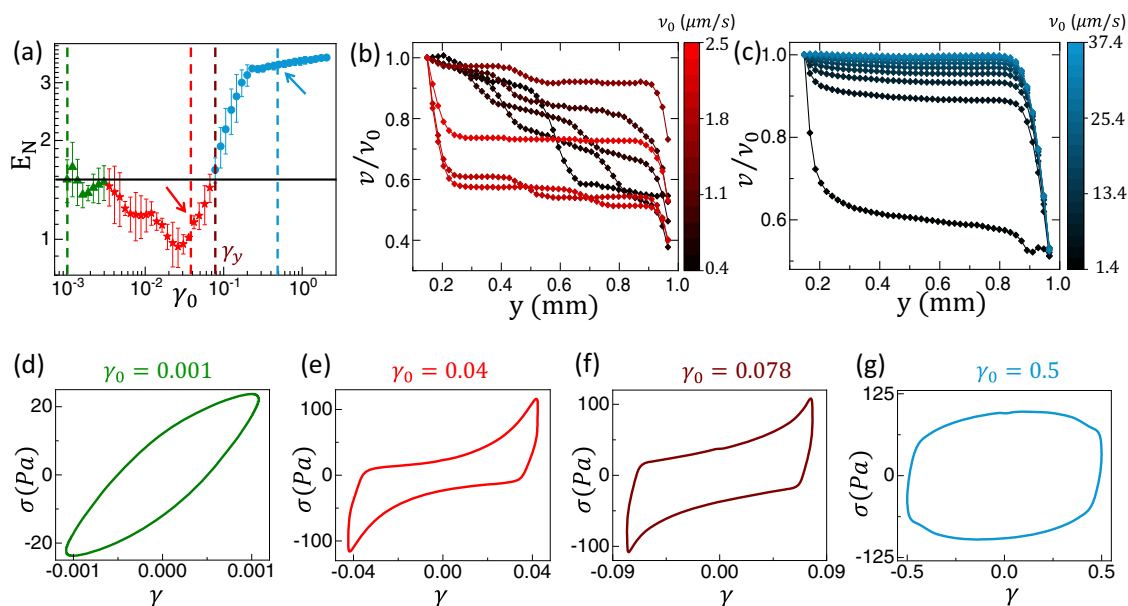


Fig. 2 Correlation between dissipation and flow profile in different strain amplitude regimes. **a** Normalized energy dissipation E_N vs. strain amplitude γ_0 for volume fraction $\phi = 0.4$. The horizontal black line indicates $E_N = E_N^0$, the average small strain value of E_N . The points for which $E_N < E_N^0$ and $E_N > E_N^0$ are marked with red stars and blue circles, respectively. The arrows indicate the γ_0 values for which the velocity profiles are shown in **(b, c)**. The yield strain value (γ_y) is also indicated in the figure. Velocity profiles across the gap between the the top cone and the bottom plate normalized by the instantaneous maximum velocity (v_0) of the moving bottom plate for $\gamma_0 = 0.04$ (panel **b**) and $\gamma_0 = 0.5$ (panel **c**). The color gradients indicate the instantaneous maximum velocity in the sample (approximately equal to the bottom plate velocity at that instant) during one quarter of an oscillatory applied strain cycle. **d–g** indicates typical Lissajous plots corresponding to different regions of the E_N vs. γ_0 curve (marked by vertical dashed lines) shown in panel **(a)**. The corresponding γ_0 values are also indicated. In panel **a** the data points indicate the mean values and the error bars denote the standard deviations of three independent measurements. The velocity profiles in panels **b, c** are for one such independent measurement.

Fig. 2a. Here, the plane of imaging is x - y with the flow direction along ' x ' and velocity gradient along ' y ' (Fig. S7). Different v_0 values are color-coded as indicated by the colourbars in the figure. Also, as the variation of v_0 is significant (0 to v_{\max}) it is difficult to show the absolute velocity profiles in the same plot for all v_0 values. Thus, in Fig. 2b, c the profiles are normalized using the corresponding v_0 values. In both the cases we observe strong shear-banding as also reported for other adhesive/attractive systems^{51,53,54}. We also observe that for $\gamma_0 = 0.04$, the velocity fluctuations are neither systematic in space nor in time (Fig. 2b), whereas, for $\gamma_0 = 0.5$ such fluctuations are absent and the velocity profiles become much more self similar, particularly, for the higher v_0 values (Fig. 2c).

We now focus on the spatio-temporal distribution of velocity gradients in the system over a complete cycle of strain deformation. We define a dimensionless gradient given by the ratio of the local velocity gradient and the average velocity gradient across the shear gap (assuming an affine deformation) measured at the same instant of time: $\frac{\delta v / \delta y}{v_0 / d}$. In Fig. 3a, b, we show space-time plots of the dimensionless velocity gradient over an entire cycle of strain deformation. We consider discrete velocity profiles across the shear-gap equally spaced in time over one full cycle of sinusoidal strain deformation for $\gamma_0 = 0.04$ (Fig. 3a) and 0.5 (Fig. 3b), respectively. Here, the horizontal axis represents the time and the vertical axis represents the position along the direction of the velocity gradient (Fig. S7). The color-coding represents the strength of the gradient. We observe that strong local gradients appear in spatio-temporally random locations for $\gamma_0 = 0.04$ (Fig. 3a), but, such gradient distribution remains smooth for $\gamma_0 = 0.5$ (Fig. 3b), except for the regions near the boundaries at the turning points. Importantly, both below and above yielding, the velocity gradient over a significant portion of the sample (away from the shearing boundaries) remains negligible. This is also evident from the slope of the velocity profiles shown in

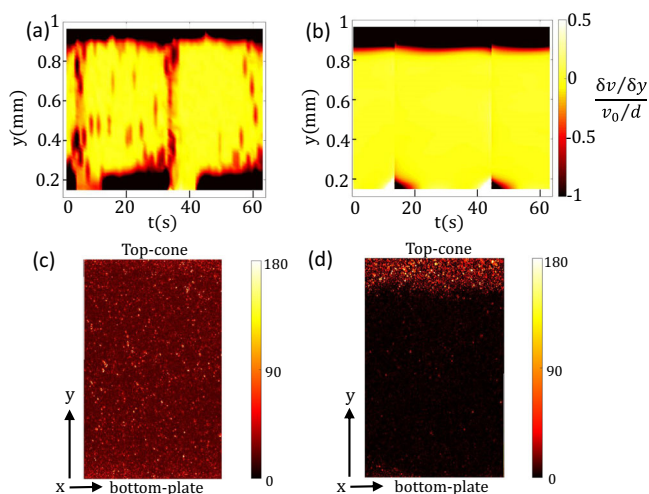


Fig. 3 Spatio-temporal velocity gradient distribution and irreversible particle rearrangements. **a, b** show the space-time plot (in y - t plane) of dimensionless velocity gradient (indicated by the colourbar) across the shear gap in the system (volume fraction $\phi = 0.4$) over a complete cycle of oscillation for strain amplitudes $\gamma_0 = 0.04$ and $\gamma_0 = 0.5$, respectively. Here, time t varies from 0 to T (time period of the applied oscillatory strain). **c, d** indicates the stroboscopic difference between images captured at applied strain $\gamma(t)$ and $\gamma(t + T)$ for $\gamma_0 = 0.04$ and $\gamma_0 = 0.5$, respectively. These results are obtained from the boundary imaging that probes a thin sample layer near the suspension-air interface.

Fig. 2b, c. This indicates that across the fluidization/yielding transition, there are coexisting solid-like and fluid-like regions inside the sample. Even deep inside the fluidized phase at large γ_0 values, such coexistence remains, with the fluidized regions confined near the shearing boundaries. We note that particularly for higher γ_0 values beyond yielding, the velocity gradient near the top cone is stronger than that near the bottom plate (Fig. 3b) as also observed for other ϕ values. Although, at high volume fractions ($\phi > 0.22$) the system forms a yield stress solid, there can still be a slight asymmetry in the strength of inter-particle contacts induced by the gravitational stress due to the density mismatch between CS and paraffin oil. Owing to the slightly weaker contacts, the suspension near the top cone gets fluidized relatively easily under a significant applied shear strain.

Next, we look at the irreversible particle reorganizations in the system by calculating stroboscopic image difference as obtained from the boundary imaging. Basically, for a given γ_0 , we calculate the difference between two gray-scale images of the sample boundary across the shear gap captured at time t and $t + T$ (Fig. S8). If the strain deformation inside the sample layer is completely reversible, such difference image should show zero intensity (within the dark-noise limit of the camera) everywhere. On the other hand, finite intensity in specific locations indicates irreversible particle rearrangements (localized plastic deformations) in the system. We see from Fig. 3c, d that irreversible rearrangements take place uniformly throughout the sample below yielding, but such events get strongly localized near the shearing boundaries for larger strain values above yielding. This behavior is strongly correlated with the velocity gradient distribution in the system (Fig. 3a, b): the plastic rearrangements predominantly take place at spatial positions where the local velocity gradients are significant, as expected.

As mentioned earlier, inter-particle interactions in dense suspensions are extremely complex and many body in nature with an intriguing dependence on the applied stress. Recent studies^{44,46} show that jamming packing fractions (ϕ_j) can be used to quantify such inter-particle interactions. To directly measure the jamming packing fractions for our system, we use particle settling experiments (see the section “Materials and methods”). Although, to our knowledge, there are no reports of such experiments to understand inter-particle interactions in adhesive granular suspensions, settling under centrifugation have been used in earlier studies to obtain insights into the rheological behaviors in repulsive frictional systems showing shear thickening^{66,67}. The basic principle of such settling experiments involves an evolution of the system from an under-constrained initial state (a suspension with relatively lower volume fraction of particles), so that, under a given forcing condition (gravity/centrifugation) the particle pack can get more and more compact and able to evolve towards the jamming packing fraction in the asymptotic/long-time limit. The jamming packing fraction for a given forcing condition is solely determined by the interparticle interactions and is invariant for a given system. The details of the settling dynamics depends on the initial volume fraction of the under-constrained state and is not important in this work, as well as, the studies mentioned earlier^{66,67}. In our case, we denote the average volume fraction inside a stable settled bed for a particular forcing condition as ϕ_{bed} that indicates the corresponding jamming packing fraction. Essentially, ϕ_{bed} is the minimum particle volume fraction required to constrain the sliding/rolling motion of the particles against the stress acting on the bed. We show the typical images of stable settled beds formed under gravity (Fig. 4a) and centrifugation at 2000 rpm (Fig. 4b) for different inter-particle interactions tuned by addition of surfactant (also see Fig. S9). We observe from Fig. 4a that for pure CS in oil system, $\phi_{\text{bed}} \approx 0.22$ that corresponds to the adhesive loose packing of the system

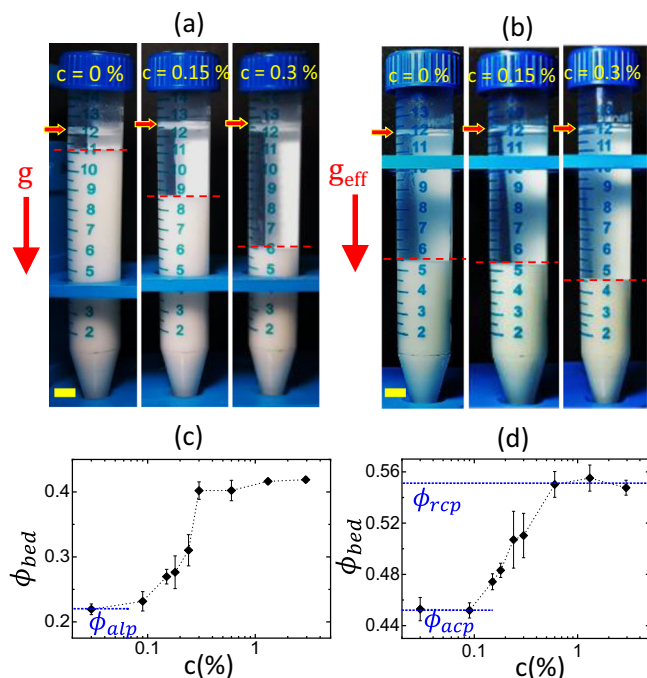


Fig. 4 Estimation of critical jamming packing fractions from particle settling experiments. **a** Stable settled bed heights obtained under gravity for different surfactant concentrations (c) as indicated in the figure. **b** Same obtained under centrifugation at a rotation rate of 2000 rpm ($g_{\text{eff}} = 455 \times g$; g : acceleration due to gravity). The red arrows indicate direction of g and g_{eff} . Each tube is marked by red-yellow arrows and dashed red lines indicating the total suspension height and the settled bed height inside the tubes, respectively. Scalebar ≈ 6.5 mm. Variation of the packing fraction inside the settled bed (ϕ_{bed}) under gravity (panel **c**) and under centrifugation at 2000 rpm (panel **d**) with increasing surfactant concentrations. In all cases the initial volume fraction of the sample is 0.2. The value of ϕ_{bed} at zero surfactant concentration under gravitational settling gives the adhesive loose packing ϕ_{alp} for the system as shown by the horizontal dashed line in **(c)**. ϕ_{bed} at zero surfactant concentration for centrifugal settling gives the adhesive close packing ϕ_{acp} and for high surfactant concentration at saturation gives the random close packing ϕ_{rcp} limit for the system, as indicated by the dashed horizontal lines in **(d)**. In **c, d** the error bars are the standard deviation and the data points represent the mean values obtained for four independent measurements.

(ϕ_{alp}). This value of ϕ_{alp} is far below the volume fraction for random close packing of CS particles having steric-repulsive interaction⁶³. This indicates a highly porous particle arrangement inside the settled bed for the adhesive system. When we add the non-ionic surfactant (Span-60) to the system, the hydrophilic part of the surfactant molecules gets adsorbed onto the surface of the particle while the hydrophobic part easily extends into the paraffin oil. With the addition of increasing amount of surfactant, the particle surface is expected to get gradually covered with enough surfactant molecules so that it becomes hydrophobic (Supplementary note 2). This effectively reduces the solvent induced adhesive interaction between the particles and makes them disperse better (see schematics in Fig. 5a–c) which leads to a disintegration of the fractal clusters resulting in a more efficient packing of the particles. As a result, the settled bed height decreases due to more compact particle organization. In Fig. 4c we show the variation of ϕ_{bed} as a function of surfactant concentration (c) for gravitational settling. With increasing c , ϕ_{bed} increases from ϕ_{alp} (for $c = 0$) and saturates beyond $c > 0.3\%$. Similar trend of ϕ_{bed} vs. c is also observed under centrifugation

(Fig. 4d), where the effective acceleration (g_{eff}) is much higher than the acceleration due to gravity (g) (see the section “Materials and methods”). We choose the value of g_{eff} such that the resulting inter-particle stress scale is much higher than that probed in the rheology measurements (see Supplementary note 3). Under this condition, ϕ_{bed} (for $c = 0$) gives the adhesive close packing (ϕ_{acp}) and the saturation at higher values of $c > 0.6\%$ gives the random close packing (ϕ_{rcp}) of the system in the limit of hard-sphere repulsion. We find $\phi_{\text{acp}} \approx 0.45$ and $\phi_{\text{rcp}} \approx 0.55$. This value of ϕ_{rcp} is close to that reported for CS particles with repulsive interactions⁶³. We also confirm that the obtained values of ϕ_{acp} and ϕ_{rcp} are not sensitive to the starting volume fractions (see Fig. S10) and the different g_{eff} values that we use. Such invariance further indicates that jamming packing fractions are directly correlated to the inter-particle interactions in the system, as mentioned above. From Fig. 4c, d, we find that the change in ϕ_{bed} as a function of surfactant concentration is much more abrupt under gravitational settling as compared to settling under centrifugation. A possible explanation can be that for the minimum amount of added surfactant, under gravitational settling the average coordination number of particles inside the settled bed (which depends on the jamming packing fraction⁴⁶) remains much lower compared to that for settling under centrifugation. Thus, beyond the critical surfactant concentration a sudden compaction is possible for gravitational settling due to lack of constraints for particle rearrangements (due to lower coordination number). However, owing to the higher coordination number, such sudden compaction is not possible for settling under centrifugation and compaction happens only gradually. However, understanding the detailed microscopic dynamics needs future studies.

Our ability to tune the inter-particle interactions enables us to investigate the role of adhesion on the observed non-linear strain stiffening and the energy dissipation in the system. In Fig. 5a–c, we show the schematics depicting how the fractal clusters of the hydrophilic particles disintegrate and finally disperse in the hydrophobic solvent with increasing surfactant concentration. From rheological measurements, we find that increasing the amount of surfactant causes a dramatic reduction of the energy dissipation (E) in the system (Fig. S11). We show the variation of E_N vs. γ_0 for $\phi = 0.35$, with different surfactant concentrations (c) in Fig. 5d. We find that the non-monotonic behavior of E_N (Fig. 5) completely disappears with the addition of sufficient amount of surfactant implying that strain stiffening also goes away under this condition (Fig. S12). This observation further confirms that adhesive interactions give rise to the non-linear strain stiffening in the system through the shear induced deformation of fractal particle clusters. Moreover, with increasing values of c , the velocity across the shearing gap also approaches a linear profile from a shear-banding one (Fig. S13).

Finally, we summarize our results for the CS in paraffin oil system using a generalized phase diagram in Fig. 6. For lower values of ϕ (below ϕ_{alp}), gravitational settling forms a bed of particles near the bottom plate and a solvent layer is observed near the top cone of the rheometer, as shown by the schematic Fig. 6a. The contact networks formed by the particles cannot span the entire gap between the shearing cone and plate, and the system behavior remains viscosity dominated over the entire range of strain amplitude (Fig. 6d). However, for values of ϕ larger than ϕ_{alp} , the settled particle bed can span the entire shear-gap (schematic Fig. 6b). The system develops a finite yield stress like a soft visco-elastic solid. In the regime $\phi > \phi_{\text{alp}}$ (but well below ϕ_{acp}), the system shows significant resistance in response to applied strain due to the stretching of adhesive contacts, however, ϕ is still low enough to not support system spanning force chains along the compression direction. Here, the system transforms

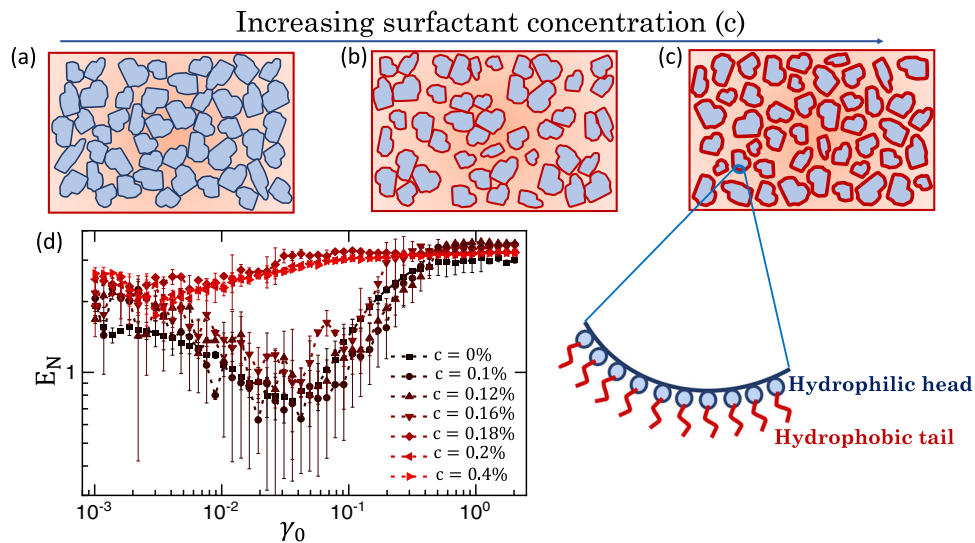


Fig. 5 Role of inter-particle adhesion on non-monotonic energy dissipation. **a–c** Schematics showing the gradual dispersion of fractal clusters with increasing surfactant concentration. The blue borders of the particles in **a** indicate the bare cornstarch (CS) particles which are hydrophilic as seen by the non-polar solvent (oil). With increasing surfactant concentration, the adsorption of the surfactant molecules on the CS particle surfaces is indicated by the increasing thickness of the red borders of the particles in **(b, c)**. We show a magnified schematic view of the surfactant adsorption in **(c)**. **d** Variation of normalized energy dissipation (E_N) as a function of strain amplitude (γ_0) for volume fraction $\phi = 0.35$ for increasing surfactant concentrations as indicated. Here, the error bars indicate standard deviation for two independent experimental runs.

from a quasi-linear visco-elastic solid to a strain-stiffening solid ($E_N < E_N^0$) and finally to a viscous/plastic material ($E_N > E_N^0$) with increasing γ_0 , as shown in Fig. 6d. We note that the strain stiffening does not take place for $\gamma_0 < 0.003$ (Fig. 6d). This indicates that significant deformation of the fractal clusters are required for the observed strain stiffening response. Also, the strain stiffening disappears for ϕ values close to ϕ_{acp} . For such high volume fractions, the system spanning force chains can also form along the compression direction (Fig. 6c)^{44,63}. Thus, strain deformations give rise to considerable frictional interaction between the particles. This results in an enhanced dissipation masking the strain stiffening response. This explains the fact that despite significant adhesive interactions, E_N remains higher than E_N^0 in this regime. Although, strain stiffening has been reported for colloidal gels formed by Brownian particles^{48,50} such complex non-monotonic variation of strain stiffening as a function of both strain amplitude and particle volume fraction have never been observed for these systems. We also observe that close to ϕ_{acp} sample mixing becomes extremely difficult and sample appears almost dry. Due to this we can not experimentally probe the regime $\phi_{acp} < \phi < \phi_{rcp}$ (Fig. 6d). Based on our present statistical accuracy, the complex nature of the phase boundaries seems to be a genuine feature of the system. Nonetheless, in future an improved statistical accuracy by considering much larger number of independent experimental runs and varying system sizes can reveal the nature of the phase boundaries more accurately. We want to reemphasize that the complex dynamics originating from the stretching/breaking of adhesive contacts and formation of frictional contacts take place near the shearing boundaries, while the bulk of the sample moves like a solid-plug as pointed out in Fig. 6b, c. This is a major addition to the existing physical picture of the flow behavior in similar systems suggested by ref. ⁴⁴.

Conclusion

We study yielding and energy dissipation in granular suspensions of adhesive frictional particles. We find that the normalized energy dissipation E_N shows a non-monotonic dependence on both applied strain amplitude (γ_0) and volume fraction (ϕ). We

show that such non-monotonic behavior is intimately linked to the interplay between inter-particle adhesion and friction in the system. From optical imaging, we observe strain localization and random spatio-temporal fluctuations in local velocity gradients. Using stroboscopic image sampling, we demonstrate a direct correlation between such fluctuations and irreversible particle rearrangements. We find that the non-monotonic variation of E_N for intermediate γ_0 values is similar to that observed for variation of system energy in poorly annealed glasses^{15,68,69}, where the applied oscillatory strain can mechanically anneal the system which can compete with the initial thermal annealing. However, contrary to the numerical studies mentioned above, for our system we observe non-monotonicity in a derived quantity E_N , but, the dissipated energy density (E) remains monotonic in γ_0 (Fig. 1d). Furthermore, we do not observe any increase in the bulk rigidity of the system for intermediate strain values as confirmed by the steady drop in G' with increasing γ_0 (Fig. 1a). This indicates that the nature of non-monotonicity observed in E_N is different from that observed in numerical studies on poorly annealed glasses. We also find that pre-shearing (mechanical annealing) does not have an effect on the non-monotonicity of E_N (Fig. S14). However, possible connection between the observed non-monotonicity in glassy and adhesive granular systems needs more detailed exploration in future.

A salient feature of our study is that we directly measure the critical jamming packing fractions using particle-settling experiments. We show that the critical jamming packing fractions, estimated from these experiments, successfully capture the essential physics behind the different flow regimes observed over a wide range of volume fractions and applied strain amplitudes. For particle settling experiments, density mismatch between the particles and the solvent is required. However, the different rheological responses like non-linear strain stiffening and plasticity are found to be quite a general feature of adhesive granular suspensions which are unaffected by gravitational effects.

We find, using stroboscopic imaging, a clear difference between irreversible particle arrangements above and below yielding: below yielding such events happen throughout the system,

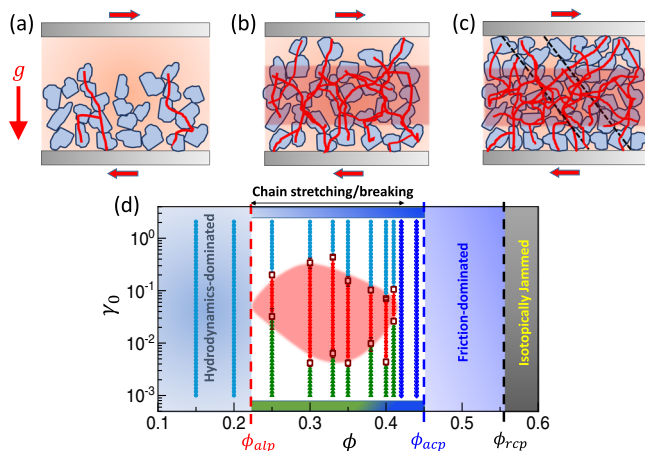


Fig. 6 Yielding phase diagram. Schematics showing the configurations under gravity for different volume fractions (ϕ) of cornstarch (CS) in Paraffin oil during the rheology measurements. **a** For volume fraction $\phi < \phi_{alp}$ (ϕ_{alp} : adhesive loose packing), the adhesive particle contacts (red solid lines) cannot span the entire gap due to settling. **b** $\phi_{alp} < \phi < \phi_{acp}$ (ϕ_{acp} : adhesive close packing) contact networks span the gap. In this region, the system forms load bearing chains under extension but not along the compression direction. For even higher ϕ values (panel **c**), such compressive force chains (dashed black lines) stabilized by inter-particle friction can also form. The shaded region midway from both the plates (panels **b, c**) indicate the solid-like region inside the sample and the red arrows indicate shearing of the sample by the cone and plate. These scenarios are summarized in a phase diagram in panel **d** in the parameter plane of ϕ and strain amplitude (γ_0). Different regions are marked based on the rheological response of the system. For $\phi < \phi_{alp}$ we get a viscous behavior (light blue circles) over the entire range of γ_0 . For $\phi_{alp} < \phi < \phi_{acp}$ we observe a non-monotonic strain response of the normalized energy dissipation E_N related to the stretching and breaking of particle chains. The data points shown by green triangles indicate the region where $E_N \approx E_N^0$ (the average small strain value of E_N); red stars indicate the region where $E_N < E_N^0$ and strain stiffening is observed; light blue circles mark the region of $E_N > E_N^0$ where the system shows progressively larger dissipation. Such non-monotonicity disappears (dark blue diamonds) near $\phi \rightarrow \phi_{acp}$, where $E_N > E_N^0$ for all values of γ_0 . $\phi = \phi_{rcp}$ indicates the random close packing for CS particles in the limit of hard-sphere repulsion. For $\phi \geq \phi_{rcp}$, the system is isotropically jammed. The critical volume fractions ϕ_{alp} , ϕ_{acp} , and ϕ_{rcp} are obtained from the particle-settling experiments. The red shaded region indicates the strain stiffening phase of the system. The dark red hollow square symbols indicate the boundary of the strain stiffening phase and the error bars at the boundaries are estimated from the standard deviation of three independent measurements indicating fuzziness associated with the strain stiffening boundaries. The horizontal bands at the top and bottom end of panel **(d)** (for $\phi_{alp} < \phi < \phi_{acp}$) indicate the regions we have not explored experimentally, but we expect a continuous behavior as indicated by the color variation in the bands similar to the neighboring data points.

whereas, above yielding they remain confined near the boundaries. To our knowledge such difference has not been reported in the context of yielding in adhesive granular suspensions. Furthermore, existing theoretical models generally assume a system-wide fluidization beyond yielding which need not be true always, as we clearly demonstrate from the coexisting solid- and fluid-like regions in these systems. Thus, our experiments put additional constraints on the recently proposed models^{43,44} of yielding in adhesive granular suspensions. As mentioned earlier, boundary imaging can probe only a thin layer of the sample near the suspension-air interface. It will be important to extend similar stroboscopic analysis for the entire system in three-dimension. For this, one can consider techniques like ultrasound velocimetry

as mentioned in ref.⁵¹. However, this remains outside the scope of the present study.

The non-linear strain stiffening observed for intermediate applied strain values is reminiscent of similar phenomena in semi-flexible biopolymer networks⁷⁰ and colloidal gels forming strand-like structures^{48,50}. Using fluorescently labeled CS particles, we indeed observe system-spanning network-like connected structures formed by fractal clusters of adhesive particles. Thus, for intermediate packing fractions, the strain stiffening can take place due to the stretching of these contacts for moderate strain values, but larger applied strains can break the contacts giving rise to enhanced plasticity and dissipation. Addition of surfactant inhibits the adhesive interactions and thus disrupts the formation of such system spanning connected structures. Consequently, no strain stiffening is observed. Importantly, the nature of strain stiffening and its complex dependence on both strain amplitude and particle volume fractions, as observed here for the granular systems, is distinct from that reported for colloidal gels. This is not surprising in view of the difference in yielding mechanism in these two classes of systems as highlighted in recent studies^{44,45}. However, a detailed phase diagram over a large parameter range similar to our study is currently lacking for colloidal gels and is a topic of future research. It is important to note that the presence of surfactant molecules on the particle surface not only reduces the interparticle adhesion, but can also significantly modify the interparticle friction coefficients. However, quantifying such effects in our system still remains a future challenge.

Our study provides a complete picture of flow and yielding behavior in dense granular suspensions of adhesive amorphous particles and can have important implications for both theoretical as well as experimental studies in future.

Materials and methods

For our measurements, the samples are prepared by dispersing Cornstarch (CS) particles (Sigma Aldrich) in Paraffin oil (SDFCL). Since, the Young's modulus of CS particles is ≈ 5 GPa, for the maximum stress scales probed in our experiments (≈ 150 Pa, see Supplementary note 3), the strain deformation produced in the particle: $\sim \frac{150 \text{ Pa}}{5 \text{ GPa}} \sim 10^{-8}$ which is negligibly small. Thus, the particles can be considered to be rigid. CS particles are hydrophilic in nature due to the presence of -OH groups on the surface⁷¹ and hence they are well dispersed in polar solvents like water. In the absence of external stress, hard-core repulsion is the only interaction present in the systems like CS in water (neglecting van der Waals interaction which is always present at very short range). Under this condition, the system is referred to as a repulsive system. When CS particles are dispersed in a non-polar solvent like paraffin oil, the particles form clusters to minimize the interactions between the surface -OH groups and the hydrophobic solvent, giving rise to a solvent-mediated attractive/adhesive interaction between the particles. The density of CS particles is ≈ 1.6 g/cc and that for the paraffin oil is ≈ 0.89 g/cc at room temperature. Despite this density mismatch, for $\phi > 0.22$, the system develops yield stress and no particle settling is observed over few days in this volume fraction range.

The CS particles are dispersed in the oil at different volume fractions ϕ ranging from 0.15 to 0.44. To prepare the samples for $\phi \leq 0.3$, CS powder is gradually added to the oil and mixed thoroughly using a magnetic stirrer. For samples with higher ϕ values, a combination of hand mixing and magnetic stirring is employed to ensure homogeneity of the sample. For density-matched adhesive suspensions, we disperse CS particles in a density-matched hydrophobic organic liquid (Cargille labs heavy liquid organic series, Cat. no. 12410, density = 1.6 ± 0.005 g/cc at room temperature) using the sample preparation method same as for CS in paraffin oil. For making the suspensions with repulsive inter-particle interactions, we disperse CS in either water or in a water-glycerol mixture having viscosity matched with the paraffin oil at room temperature (25 °C). The suspensions prepared using water-glycerol mixture are sonicated for 20–30 min after hand mixing to ensure homogeneity. To tune the inter-particle adhesive interactions, we use a nonionic surfactant Span® 60 (Sigma Aldrich). To make the CS suspensions in oil with added surfactant, we first weigh out the required amount of surfactant (in powder form) and then crush it in a mortar pestle to get rid of big clusters, if any. Next, CS particles are added and dry mixed thoroughly with the surfactant. After that, the oil is added to the dry mixture and then the sample is mixed well in the mortar pestle followed by mixing with a magnetic stirrer till homogenized. All the samples are degassed overnight under vacuum at room temperature in a desiccator (Borosil)/vacuum oven (Allied Scientific) before rheology/particle settling experiments.

For particle settling experiments, the degassed samples are first transferred to 15 mL graduated Falcon tubes very gently. Next, the tubes are either kept in a vertical position and left undisturbed for 3 weeks (for settling under gravity) or, centrifuged (Remi, R-8C BL) in a swinging-bucket type holder with rotation speed varying between 1000 and 2500 rpm for 2 h. For this range of rotation speeds and considering slight sample to sample variation in bed heights, we find that the average acceleration approximately varies between 114g and 711g (g: acceleration due to gravity). We confirm that in all cases the waiting time is sufficient to get a stable bed formation.

For confocal microscopy, we use the fluorescent ink extracted from Faber Castell Textliner Supefluorescent markers as the dye. The excitation and emission wavelengths are 435 and 570 nm, respectively, as obtained from the absorption (using UV-visible spectroscopy, Perkin Elmer Lambda 35) and the emission spectrum (using Photoluminescence spectroscopy, Horiba Jobin Yvon-Edison, NJ USA). Sample preparation for confocal microscopy involves adding the CS particles to a petri dish containing the dye dissolved in ethanol. The solvent is then evaporated at room temperature to get the dyed CS particles. The particles are dried further in a vacuum oven. For making dense suspensions using these dyed CS particles dispersed in oil (with/without surfactant) we follow a similar mixing protocol as described above. For confocal imaging we use a Leica DMI6000 microscope and a confocal scanner (Sp8 Germany). The z-stack images are obtained with a z-spacing of 0.68 μm .

Rheological measurements are performed using a stress controlled rheometer (MCR-702 Anton Paar, Austria). We use a cone-plate geometry with diameter of 50 mm and cone angle of 2°. Both the surfaces are sand-blasted to minimize slippage at the sample boundaries. We use Large amplitude oscillatory shear (LAOS) protocol for all our rheological measurements in the separate motor transducer (SMT) mode, where the bottom plate is moving and the top cone is held stationary. LAOS measurements are done at an angular frequency (ω) of 0.1 rad/s. The rheometer measures the intra-cycle stress and strain to measure the G' and G'' values (first harmonics) for each data point of the measurement over a strain amplitude range of 0.001–2 (we have also checked over a range 0.0001–2 which we show in Fig. S2). We acquire 15 data points per decade of strain variation for the strain range of 0.001–2 and 12 points per decade for the strain range of 0.0001–2. LAOS measurements also provide higher harmonic values of the moduli. For the rheological measurements on repulsive systems (using water-glycerol mixture as solvent), an in-house built humidity chamber is used to prevent solvent evaporation. For LAOS measurements, after loading the sample in the cone-plate geometry, we wait for the normal force response from the loaded sample to reach zero before starting the measurements. We observe that for $\phi \leq 0.3$, the normal force almost immediately goes to zero, but for higher ϕ values, we have to wait for a few minutes before the normal force vanishes. We find that this protocol provides a fairly good reproducibility, as seen from the multiple independent experimental runs (Fig. S14a and S14b). Although we did not apply any pre-shear to our samples, we verified that applying a pre-shear before the measurements does not significantly alter the results (Fig. S14c).

The in-situ imaging is done using a Lumenera Lt545R camera fitted with a 5X Mitutoyo objective. For image analysis, the images are taken at discrete values of γ_0 with frame rate varying between 1 and 40 Hz.

Data availability

The data types used in the manuscript and supplementary materials are in: .DAT format (text data), .JPG format (image data) and .MP4 format (movie data). All data corresponding to the reported results are available from the corresponding author under reasonable request.

Received: 22 June 2021; Accepted: 5 May 2022;

Published online: 26 May 2022

References

- Falk, M. L. & Langer, J. S. Deformation and failure of amorphous, solidlike materials. *Annu. Rev. Condens. Matter Phys.* **2**, 353–373 (2011).
- Berthier, L., Biroli, G., Bouchaud, J.-P., Cipelletti, L. & van Saarloos, W. *Dynamical Heterogeneities in Glasses, Colloids, and Granular Media*: Vol. 150. *International Series of Monographs on Physics* (OUP Oxford, 2011).
- Bonn, D., Denn, M. M., Berthier, L., Divoux, T. & Manneville, S. Yield stress materials in soft condensed matter. *Rev. Mod. Phys.* **89**, 035005 (2017).
- Coussot, P. Yield stress fluid flows: a review of experimental data. *J. Non-Newton. Fluid Mech.* **211**, 31–49 (2014).
- Bera, P. K., Majumdar, S., Ouillon, G., Sornette, D. & Sood, A. K. Quantitative earthquake-like statistical properties of the flow of soft materials below yield stress. *Nat. Commun.* **11**, 1–9 (2020).
- Jerolmack, D. J. & Daniels, K. E. Viewing earth's surface as a soft-matter landscape. *Nat. Rev. Phys.* **1**, 716–730 (2019).
- van der Vaart, K. et al. Rheology of concentrated soft and hard-sphere suspensions. *J. Rheol.* **57**, 1195 (2013).
- Patinet, S., Vandembroucq, D. & Falk, M. L. Connecting local yield stresses with plastic activity in amorphous solids. *Phys. Rev. Lett.* **117**, 045501 (2016).
- Richard, D. et al. Predicting plasticity in disordered solids from structural indicators. *Phys. Rev. Mater.* **4**, 113609 (2020).
- Lin, J., Lerner, E., Rosso, A. & Wyart, M. Scaling description of the yielding transition in soft amorphous solids at zero temperature. *Proc. Natl Acad. Sci. USA* **111**, 14382–14387 (2014).
- Ghosh, A. et al. Direct observation of percolation in the yielding transition of colloidal glasses. *Phys. Rev. Lett.* **118**, 148001 (2017).
- Koumakis, N. & Petekidis, G. Two step yielding in attractive colloids: transition from gels to attractive glasses. *Soft Matter* **7**, 2456–2470 (2011).
- Pham, K. et al. Yielding of colloidal glasses. *Europhys. Lett.* **75**, 624 (2006).
- Grenard, V., Divoux, T., Taberlet, N. & Manneville, S. Timescales in creep and yielding of attractive gels. *Soft Matter* **10**, 1555–1571 (2014).
- Leishangthem, P., Parmar, A. D. S. & Sastry, S. The yielding transition in amorphous solids under oscillatory shear deformation. *Nat. Commun.* **8**, 1–8 (2017).
- Karmakar, S., Lerner, E. & Procaccia, I. Statistical physics of the yielding transition in amorphous solids. *Phys. Rev. E* **82**, 055103 (2010).
- Maloney, C. E., & Lemaitre, A. Amorphous systems in athermal, quasistatic shear. *Phys. Rev. E* **74**, 016118 (2006).
- Keim, N. C. & Arratia, P. E. Yielding and microstructure in a 2D jammed material under shear deformation. *Soft Matter* **9**, 6222–6225 (2013).
- Denisov, D., Lörincz, K., Uhl, J., Dahmen, K. & Schall, P. Universality of slip avalanches in flowing granular matter. *Nat. Commun.* **7**, 1–6 (2016).
- Jaiswal, P. K., Procaccia, I., Rainone, C. & Singh, M. Mechanical yield in amorphous solids: a first-order phase transition. *Phys. Rev. Lett.* **116**, 085501 (2016).
- Regev, I., Weber, J., Reichhardt, C., Dahmen, K. A. & Lookman, T. Reversibility and criticality in amorphous solids. *Nat. Commun.* **6**, 1–8 (2015).
- Knowlton, E. D., Pine, D. J. & Cipelletti, L. A microscopic view of the yielding transition in concentrated emulsions. *Soft Matter* **10**, 6931–6940 (2014).
- Shrivastav, G. P., Chaudhuri, P. & Horbach, J. Yielding of glass under shear: a directed percolation transition precedes shear-band formation. *Phys. Rev. E* **94**, 042605 (2016).
- Nicolas, A., Ferrero, E. E., Martens, K. & Barrat, J.-L. Deformation and flow of amorphous solids: insights from elastoplastic models. *Rev. Mod. Phys.* **90**, 045006 (2018).
- Sastry, S. Models for the yielding behaviour of amorphous solids. *Phys. Rev. Lett.* **126**, 255501 (2021).
- Zhao, Y., Barés, J. & Socolar, J. E. Yielding, rigidity, and tensile stress in sheared columns of hexapod granules. *Phys. Rev. E* **101**, 062903 (2020).
- Barlow, H. J., Cochran, J. O. & Fielding, S. M. Ductile and brittle yielding in thermal and athermal amorphous materials. *Phys. Rev. Lett.* **125**, 168003 (2020).
- Donley, G. J., de Bruyn, J. R., McKinley, G. H. & Rogers, S. A. Time-resolved dynamics of the yielding transition in soft materials. *J. Non-Newton. Fluid Mech.* **264**, 117–134 (2019).
- Dijksman, J. A., Wortel, G. H., van Dellen, L. T., Dauchot, O. & van Hecke, M. Jamming, yielding, and rheology of weakly vibrated granular media. *Phys. Rev. Lett.* **107**, 108303 (2011).
- Liu, C., Dutta, S., Chaudhuri, P. & Martens, K. Elastoplastic approach based on microscopic insights for the steady state and transient dynamics of sheared disordered solids. *Phys. Rev. Lett.* **126**, 138005 (2021).
- Liu, A. J. & Nagel, S. R. Jamming is not just cool any more. *Nature* **396**, 21–22 (1998).
- Fall, A., Huang, N., Bertrand, F., Ovarlez, G. & Bonn, D. Shear thickening of cornstarch suspensions as a reentrant jamming transition. *Phys. Rev. Lett.* **100**, 018301 (2008).
- Seto, R., Singh, A., Chakraborty, B., Denn, M. M. & Morris, J. F. Shear jamming and fragility in dense suspensions. *Granul. Matter* **21**, 82–8 (2019).
- Vázquez-Quesada, A., Tanner, R. & Ellero, M. Shear thinning of noncolloidal suspensions. *Phys. Rev. Lett.* **117**, 108001 (2016).
- Brown, E. & Jaeger, H. M. Shear thickening in concentrated suspensions: phenomenology, mechanisms and relations to jamming. *Rep. Prog. Phys.* **77**, 046602 (2014).
- Cheng, X., McCoy, J. H., Israelachvili, J. N. & Cohen, I. Imaging the microscopic structure of shear thinning and thickening colloidal suspensions. *Science* **333**, 1276–1279 (2011).
- Dhar, S., Chattopadhyay, S. & Majumdar, S. Signature of jamming under steady shear in dense particulate suspensions. *J. Phys.: Condens. Matter* **32**, 124002 (2019).
- Fall, A., Bertrand, F., Ovarlez, G. & Bonn, D. Yield stress and shear banding in granular suspensions. *Phys. Rev. Lett.* **103**, 178301 (2009).
- Perrin, H., Clavaud, C., Wyart, M., Metzger, B. & Forterre, Y. Interparticle friction leads to nonmonotonic flow curves and hysteresis in viscous suspensions. *Phys. Rev. X* **9**, 031027 (2019).

40. Forterre, Y. & Pouliquen, O. Flows of dense granular media. *Annu. Rev. Fluid Mech.* **40**, 1–24 (2008).
41. Guy, B., Hermes, M. & Poon, W. C. Towards a unified description of the rheology of hard-particle suspensions. *Phys. Rev. Lett.* **115**, 088304 (2015).
42. Koeze, D. J. & Tighe, B. P. Sticky matters: jamming and rigid cluster statistics with attractive particle interactions. *Phys. Rev. Lett.* **121**, 188002 (2018).
43. Guy, B., Richards, J., Hodgson, D., Blanco, E. & Poon, W. Constraint-based approach to granular dispersion rheology. *Phys. Rev. Lett.* **121**, 128001 (2018).
44. Richards, J. A. et al. The role of friction in the yielding of adhesive non-Brownian suspensions. *J. Rheol.* **64**, 405 (2020).
45. Richards, J. A., O'Neill, R. E. & Poon, W. C. K. Turning a yield-stress calcite suspension into a shear-thickening one by tuning inter-particle friction. *Rheologica Acta.* **60**, 97 (2021).
46. Singh, A., Ness, C., Seto, R., de Pablo, J. J. & Jaeger, H. M. Shear thickening and jamming of dense suspensions: the “roll” of friction. *Phys. Rev. Lett.* **124**, 248005 (2020).
47. Wyart, M. & Cates, M. Discontinuous shear thickening without inertia in dense non-brownian suspensions. *Phys. Rev. Lett.* **112**, 098302 (2014).
48. Gislser, T., Ball, R. C. & Weitz, D. A. Strain hardening of fractal colloidal gels. *Phys. Rev. Lett.* **82**, 1064 (1999).
49. Colombo, J. & Del Gado, E. Stress localization, stiffening, and yielding in a model colloidal gel. *J. Rheol.* **58**, 1089–1116 (2014).
50. van Doorn, J. M., Verweij, J. E., Sprakel, J. & van der Gucht, J. Strand plasticity governs fatigue in colloidal gels. *Phys. Rev. Lett.* **120**, 208005 (2018).
51. Bécu, L., Manneville, S. & Colin, A. Yielding and flow in adhesive and nonadhesive concentrated emulsions. *Phys. Rev. Lett.* **96**, 138302 (2006).
52. Schall, P. & Van Hecke, M. Shear bands in matter with granularity. *Annu. Rev. Fluid Mech.* **42**, 67–88 (2010).
53. Liberto, T., Le Merrer, M., Manneville, S. & Barentin, C. Interparticle attraction controls flow heterogeneity in calcite gels. *Soft Matter* **16**, 9217–9229 (2020).
54. Irani, E., Chaudhuri, P. & Heussinger, C. Impact of attractive interactions on the rheology of dense athermal particles. *Phys. Rev. Lett.* **112**, 188303 (2014).
55. Irani, E., Chaudhuri, P. & Heussinger, C. Athermal rheology of weakly attractive soft particles. *Phys. Rev. E* **94**, 052608 (2016).
56. Chaudhuri, P., Berthier, L. & Bocquet, L. Inhomogeneous shear flows in soft jammed materials with tunable attractive forces. *Phys. Rev. E* **85**, 021503 (2012).
57. Vasisht, V. V., Roberts, G. & Del Gado, E. Emergence and persistence of flow inhomogeneities in the yielding and fluidization of dense soft solids. *Phys. Rev. E* **102**, 010604 (2020).
58. Singh, M., Ozawa, M. & Berthier, L. Brittle yielding of amorphous solids at finite shear rates. *Phys. Rev. Mater.* **4**, 025603 (2020).
59. Waitukaitis, S. R. *Impact-activated Solidification of Cornstarch and Water Suspensions* (Springer, 2014).
60. Neidhöfer, T., Wilhelm, M. & Spiess, H. W. Fourier-transform-rheology on linear polystyrene melts. *Appl. Rheol.* **11**, 126–133 (2001).
61. Trappe, V., Prasad, V., Cipelletti, L., Segre, P. N. & Weitz, D. A. Jamming phase diagram for attractive particles. *Nature* **411**, 772–775 (2001).
62. Maxwell, J. C. L. On the calculation of the equilibrium and stiffness of frames. *Lond. Edinb. Dublin Philos. Mag. J. Sci.* **27**, 294–299 (1864).
63. Peters, I. R., Majumdar, S. & Jaeger, H. M. Direct observation of dynamic shear jamming in dense suspensions. *Nature* **532**, 214–217 (2016).
64. Schreuders, F. et al. Small and large oscillatory shear properties of concentrated proteins. *Food Hydrocoll.* **110**, 106172 (2021).
65. Fernandes, R. R., Andrade, D. E. V., Franco, A. T. & Negrão, C. O. R. The yielding and the linear-to-nonlinear viscoelastic transition of an elastoviscoplastic material. *J. Rheol.* **61**, 893 (2017).
66. Fernandez, N. et al. Microscopic mechanism for shear thickening of non-brownian suspensions. *Phys. Rev. Lett.* **111**, 108301 (2013).
67. Hsu, C.-P., Ramakrishna, S. N., Zanini, M., Spencer, N. D. & Isa, L. Roughness-dependent tribology effects on discontinuous shear thickening. *Proc. Natl Acad. Sci. USA* **115**, 5117–5122 (2018).
68. Liu, C. et al. The fate of shear-oscillated amorphous solids. *J. Chem. Phys.* **156**, 104902 (2022).
69. Yeh, W.-T., Ozawa, M., Miyazaki, K., Kawasaki, T. & Berthier, L. Glass stability changes the nature of yielding under oscillatory shear. *Phys. Rev. Lett.* **124**, 225502 (2020).
70. Storm, C., Pastore, J. J., MacKintosh, F. C., Lubensky, T. C. & Janmey, P. A. Nonlinear elasticity in biological gels. *Nature* **435**, 191–194 (2005).
71. James, N. M., Han, E., de la Cruz, R. A. L., Jureller, J. & Jaeger, H. M. Interparticle hydrogen bonding can elicit shear jamming in dense suspensions. *Nat. Mater.* **17**, 965–970 (2018).

Acknowledgements

S.M. thanks SERB (under DST, Govt. of India) for a Ramanujan Fellowship. We acknowledge Ivo Peters for developing the Matlab codes used for PIV analysis, K.M. Yatheendran for help with the SEM imaging and RRI workshop facility for machining the humidity chamber. We thank Pinaki Chaudhuri for helpful discussion.

Author contributions

S.C. and S.M. designed the research, S.C. and S.N. performed the experiments, S.C., S.N., and S.M. analyzed the data. S.C. and S.M. wrote the manuscript.

Competing interests

The authors declare no competing interests.

Additional information

Supplementary information The online version contains supplementary material available at <https://doi.org/10.1038/s42005-022-00904-4>.

Correspondence and requests for materials should be addressed to Sayantan Majumdar.

Peer review information Communications Physics thanks Jie Zhang, Ezequiel Ferrero and the other, anonymous, reviewer(s) for their contribution to the peer review of this work. Peer reviewer reports are available.

Reprints and permission information is available at <http://www.nature.com/reprints>

Publisher's note Springer Nature remains neutral with regard to jurisdictional claims in published maps and institutional affiliations.

 **Open Access** This article is licensed under a Creative Commons Attribution 4.0 International License, which permits use, sharing, adaptation, distribution and reproduction in any medium or format, as long as you give appropriate credit to the original author(s) and the source, provide a link to the Creative Commons license, and indicate if changes were made. The images or other third party material in this article are included in the article's Creative Commons license, unless indicated otherwise in a credit line to the material. If material is not included in the article's Creative Commons license and your intended use is not permitted by statutory regulation or exceeds the permitted use, you will need to obtain permission directly from the copyright holder. To view a copy of this license, visit <http://creativecommons.org/licenses/by/4.0/>.

© The Author(s) 2022